Article:
MATHARU, AVTAR SINGH, Gao, Yang, Ji, Ruipeng et al. (2026) From lignocellulosic nanofibres isolated using ternary deep eutectic solvents to composite hydrogels for efficient tetracycline removal. ACS Sustainable Resource Management. ISSN: 2837-1445

https://doi.org/10.1021/acssusresmgt.6c00244

ACS Sustainable Resource Management

pubs.acs.org/acssrm

Article

From Lignocellulosic Nanofibres Isolated Using Ternary Deep Eutectic Solvents to Composite Hydrogels for Efficient Tetracycline Removal

Yang Gao,* Ruipeng Ji, Ziyi Ren, Zhicheng Jiang, Shichao Xu,* and Avtar S. Matharu*

Cite This: https://doi.org/10.1021/acssusresmgt.6c00244

Read Online

ACCESS | Metrics & More | Article Recommendations | Supporting Information

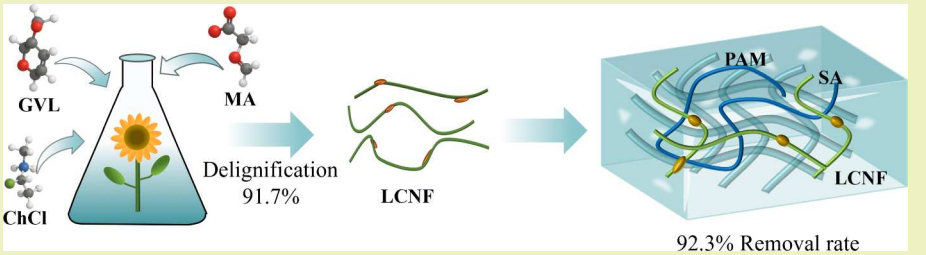

ABSTRACT: The removal of residual antibiotics, such as tetracycline (TC), from the environment is an important global grand challenge to combat an ever-increasing prevalence of antimicrobial resistance (AMR). Herein, a novel ternary deep eutectic solvent (DES) comprising choline chloride (ChCl), γ-valerolactone (GVL), and maleic acid (MA) was used to produce lignocellulosic nanofibers (LCNFs) from sunflower stalks, which, when combined with sodium alginate (SA) and polyacrylamide (PAM), afforded hydrogels for the efficient removal of TC. The ternary ChCl/MA/GVL DES was highly effective for lignin removal (delignification efficiency, 91.70%). The physical properties of the LCNFs could be tailored with respect to temperature, i.e., with increasing temperature, the lignin content ranged from 4.90 to 25.90%, the crystallinity index (CrI) ranged from 31.85 to 45.66%, and size dispersity ranged from 11.47 to 31.29 nm. The incorporation of obtained LCNF into PAM/SA hydrogels significantly enhanced their adsorption performance (92.3 vs 72.96%) for TC. Kinetic adsorption experiments revealed that chemical adsorption was the main mechanism dominating TC removal, and the pseudo-second-order model (Q_e = 79.24 mg·g^{-1}) was considerably closer to the experimental result (Q_e = 69.71 mg·g^{-1}). The interactions between the adsorbent and the adsorbate were investigated using the Langmuir and Freundlich models. The Langmuir model exhibited higher R^2 values (0.981, 0.986, and 0.989) in comparison with the Freundlich model (0.937, 0.948, and 0.953), suggesting that TC adsorption occurs via a monolayer process, with adsorption sites evenly distributed on the surface of hydrogels. The Freundlich constants were approximately 2.3, demonstrating the thermodynamic favorability of the adsorption process. The incorporation of LCNFs enhanced the removal rate of TC to a maximum of 92.3%, and the hydrogel still maintains relatively high adsorption capacity (49.87 mg·g^{-1}) and removal rate (62.34%) for TC after four cycles. These findings demonstrate a practical approach to employing LCNFs for removing tetracycline antibiotics from water, thus contributing to the fight against AMR.

KEYWORDS: *lignocellulosic nanofibers, deep eutectic solvents, tetracycline removal, isotherm models*

1. INTRODUCTION

Combating antimicrobial resistance (AMR) caused by the overuse and poor management of antibacterial agents is recognized as a grand global challenge due to its adverse effects on public health, biodiversity, and Sustainable Development Goals (SDGs).[1,2] The increasing incidence of zoonotic diseases recently has led to a surge in pharmaceutical use, raising significant concerns regarding the ecological safety of water resources.[3−5] Tetracycline, a commonly used antibiotic, poses potential risks to the environment and human health because of its significant bioaccumulation potential, persistence, and resistance to biodegradation.[6,7] This situation not only jeopardizes human health but also exacerbates antibiotic resistance within aquatic bacterial populations.[8] Consequently, globally concerted efforts are aimed at the elimination of tetracycline from water environments.[9]

Received: April 17, 2026
Revised: July 2, 2026
Accepted: July 2, 2026

Various methods, including advanced oxidation processes,[10] membrane separation,[11−13] photocatalytic degradation,[14−16] and adsorption techniques,[17−19] have been employed to address tetracycline pollution. Among these, adsorption is particularly attractive owing to its low cost, ease of operation, and feasibility of regeneration.[20] Sodium alginate (SA) and polyacrylamide (PAM) hydrogels are promising natural adsorbents, characterized by their nontoxicity, biodegradability, and low cost.[21,22] Nevertheless, the cross-linking of these two polymers led to reduced exposure of active sites (e.g., carboxylic acid groups) and a low specific surface area, which inhibits their further utilization.[23] Therefore, by integrating other substances into a base materials matrix, the fabrication of composite materials has attracted widespread interest from researchers due to their cost-effectiveness and greater adsorption efficiency.[24]

Among various additives, lignocellulosic nanofibers (LCNFs) extracted from lignocellulose biomass exhibit promising potential because of their unique nanostructure (high surface area and superior mechanical properties) and environmentally friendly characteristics (biodegradability and renewability).[25] Compared with pure cellulose, LCNFs retain a certain amount of lignin, which is rich in phenolic hydroxyl, aliphatic hydroxyl, methoxy, aromatic, and carboxyl groups. These functionalities provide abundant potential binding sites for TC and promote adsorption through electrostatic interactions, ion exchange, hydrogen bonding, and π–π interaction effects. In addition, the hydrophobic aromatic structures of lignin alleviate the self-aggregation of cellulose nanofibrils induced by intermolecular hydrogen bonding, leading to a more porous network structure and greater exposure of active adsorption sites. The introduction of LCNFs as a reinforcing agent not only facilitates the formation of robust physical entanglements and networks within composite materials but also enhances the hydrogel's adsorption capacity.[26,27] Despite the advancements of LCNFs as potential composites, the recalcitrance of lignocellulose within the complex, cross-linked structure continues to severely limit its extraction and downstream valorization.[28,29]

Deep eutectic solvent (DES) systems are considered a promising pretreatment method for lignocellulose owing to their facile preparation, nonvolatility, low cost, and recyclability.[30−32] Previous studies have demonstrated that DES systems can effectively disrupt lignin–carbohydrate complexes and facilitate the preparation of LCNFs, such as choline chloride/acetic acid,[32] choline chloride/formic acid,[33] choline chloride/urea,[34] choline chloride/glyoxylic acid,[35] choline chloride/urea lactic acid,[36,37] and choline chloride/urea/toluenesulfonic acid.[38] However, binary DES systems continue to face key challenges, including high viscosity and undesirable condensation under acidic conditions, which impede mass transfer and structural degradation, thereby hindering downstream valorization.[39] Recent efforts have focused on incorporating a third component to improve mass transfer, mitigate undesirable side reactions during pretreatment, and enhance overall output.[40,41] γ-Valerolactone (GVL) is a green solvent known for its excellent solvation properties and stability.[42,43] The incorporation of GVL into DES effectively reduces viscosity, stabilizes reactive intermediates (such as benzylic carbocations), and inhibits condensation reactions.[44] For instance, Cheng et al. highlighted the effectiveness of the DES/GVL solvent for delignification (88.61%) and xylan removal (98.67%), while also preserving the structure of the recovered lignin.[45] Morais et al. observed that the incorporation of GVL in DES contributed to improved yields (89.5%) for furfural production from xylan. Yao et al. achieved both high lignin extraction efficiency (71.35% from poplar) and cellulose retention (92.87%) using the ChCl/5-sulfosalicylic acid/GVL system.[46] Yu et al. further demonstrated the efficacy of ChCl/LA/GVL in removing lignin from tobacco stems.[47] However, extensive research of DES/GVL has focused on furfural production and delignification; the role of DES/GVL systems in delignification performance and the structural characteristics of the resultant LCNFs have not been thoroughly explored. Furthermore, the influence of DES composition on the surface chemistry and microstructure of LCNFs, as well as its effect on antibiotic adsorption mechanisms, remains unexplored.

Herein, maleic acid (MA), a biomass-derived organic acid, which can efficiently separate lignin with lower condensation,[48] was selected to form a novel ternary choline chloride/maleic acid/γ-valerolactone DES system to prepare LCNFs from sunflower stalks, a renewable resource. The LCNFs are then compounded with SA and PAM to fabricate a high-performance hydrogel adsorbent for TC adsorption from wastewater. The structural, morphological, and physicochemical characteristics of hydrogels are systematically characterized, and the adsorption performance towards tetracycline is investigated in detail. According to our current knowledge, related studies remain limited; the present work thereby provides a sustainable strategy for the utilization of lignocellulosic feedstocks, as well as for developing a promising bio-based adsorbent for water remediation.

2. MATERIALS AND METHODS

2.1. Chemicals

All chemicals and solvents (maleic acid, choline chloride, GVL, sodium alginate, acrylamide, ammonium persulfate (APS), *N, N′*-methylenebisacrylamide (MBA), aluminum chloride hexahydrate, ethanol, and tetracycline) used were of reagent grade and purchased from Macklin (China). Deionized water was utilized in all experiments.

2.2. Synthesis of Ternary DES

Prior to synthesis, choline chloride was dried in vacuum (80 °C for 6 h) to remove moisture and then stored. The DES was obtained through mixing ChCl, GVL and MA in a round-bottom flask (250 mL) with a molar ratio of 1.1:1:1 immersed in a 90 °C oil heating bath and then stirred (500 rpm) until a transparent solution was obtained. The solutions were then cooled to ambient temperature.

2.3. Preparation of LCNFs

Sunflower cornstalks were collected in Tianjin, China, and dried at 100 °C overnight. The stalks were milled and sieved using a 60-mesh screen and then boiled with ethanol for 4 h to remove the organic compounds. The extracted material was then dried and stored in airtight containers. Based on previous preliminary experiments, 2.5 g powders were added to 50 mL DES and then stirred in a flask at temperatures ranging from 100 to 160 °C for 5 h. The mixtures were then cooled and separated by vacuum filtration. The collected solid residues were washed with hot water and ethanol until neutral pH was achieved to minimize the presence of residual DES components and soluble byproducts and subjected to vacuum filtration and homogenized (20,000 rpm, 5 min) for subsequent characterization. All samples were labeled as CMG100, CMG120, CMG140, and CMG160, corresponding to the temperatures used. The solid recovery, delignification efficiency, and xylan removal were calculated according to eqs. 1–3, respectively.

$$\text{Solid recovery}\ (\%) = \frac{\text{sample after pretreatment}}{\text{raw material}} \times 100\% \quad (1)$$

https://doi.org/10.1021/acssusresmgt.6c00244
ACS Sustainable Resour. Manage. XXXX, XXX, XXX−XXX

$$\text{Delignification efficiency} = \frac{\%\ \text{of lignin (raw material)} - \%\ \text{of lignin (sample after pretreatment)}}{\%\ \text{of lignin (raw material)}} \times 100\% \quad (2)$$

$$\text{Xylan removal}\ (\%) = \frac{\%\ \text{of xylan (raw material)} - \%\ \text{of xylan (sample after pretreatment)}}{\%\ \text{of xylan (raw material)}} \times 100\% \quad (3)$$

2.4. Structural Analysis of LCNFs

The chemical and structural composition of the sunflower stalks and resultant LCNFs were analyzed based on National Renewable Energy Laboratory methods. Fourier transform infrared (FT-IR) spectra of LCNFs were acquired with Nicolet iSTM5 (Thermo Scientific, Waltham, MA, USA) ranging from 500 to 4000 cm^{-1}. X-ray diffractometry (XRD) was conducted on an Ultima-185 diffractometer (Rigaku, Tokyo, Japan) Solid-state ^{13}C cross-polarization magic-angle spinning NMR spectra were collected using a Bruker Avance NEO 400WB spectrometer (Bruker, Germany). Thermal decomposition property was analyzed using a TG 209F3 Tarsus thermogravimetric analyzer (Netzsch, Selb, Germany). The crystallinity index (CrI) was determined by integrating the areas corresponding to the amorphous (80–86 ppm) and crystalline (86–92 ppm) regions, according to eq 4.[49]

$$\text{CrI} = \frac{A_{89-92\text{ppm}}}{A_{86-92\text{ppm}} + A_{80-86\text{ppm}}} \quad (4)$$

Morphology and particle size distributions were obtained using a MIRA LMS field-emission scanning electron microscope (SEM, TESCAN, Czech Republic) and JEM-F200 (TEM, JEOL Japan). A Nanobrook Omni analyzer (Brookhaven Instruments, USA) was used to obtain zeta potential values of LCNFs. All experiments were performed three times to ensure accuracy. Detailed information is shown in ESI 1.1.

2.5. Synthesis and Characterization of the PAM/SA/LCNF Hydrogel

Precisely 0.1 g of CMG140 was dissolved in 500 mL of water and then subjected to ultrasonication (15 min) to prepare a 0.2% (w/v) aqueous solution. SA (0.5 g) was added to the dispersion at 40 °C for 30 min until complete dissolution. Subsequently, 3 g of acrylamide (AM) was introduced and stirred for another 40 min. Then, 0.06 g of APS (initiator) and 0.02 g of MBA (cross-linker) were added and stirred for 30 min to facilitate complete cross-linking. The solution was ultrasonicated for 10 min to remove bubbles and transferred into a 1% aqueous aluminum chloride solution for curing to obtain the hydrogel, denoted as PAM/SA/LCNF (ESI Figure S1). The PAM/SA/LCNF hydrogel was freeze-dried for subsequent batch adsorption experiments. As a control, the PAM/SA hydrogel without LCNF was prepared using the same procedure. When used for adsorbing TC, 15 mg of adsorbent was introduced into 20 mL of TC solution (60 $mg{\cdot}L^{-1}$) and stirred for 12 h.

2.6. Batch Adsorption Experiment

The experiments involved the following: (1) Adsorption isotherm study: Initial TC concentrations were varied from 60 to 180 $mg{\cdot}L^{-1}$, and the adsorption temperature was set at 25, 35, and 45 °C. (2) Effect of dosage: The dosage of hydrogel ranged from 5 to 25 mg, with the temperature maintained at 25 °C. (3) Effect of time: The time ranged from 0 to 1440 min. (4) Effect of concentration: The initial TC concentrations were set at 60, 80, 100, 120, 140, 160, and 180 $mg{\cdot}L^{-1}$, respectively. (5) Effect of temperature: The temperatures were set at 25, 30, 35, 40, and 45 °C. (6) Adsorption kinetics investigation: The concentration was 60 $mg{\cdot}L^{-1}$, with adsorption times of 10, 60, 120, 180, 240, 300, 360, and 420 min. (7) Reusability and reproducibility of the hydrogel: Following the adsorption process, the adsorbed hydrogel was collected and subjected to desorption by separately adding it to ethanol and 0.1 $mol{\cdot}L^{-1}$ NaOH desorption solutions. The hydrogel was washed with deionized water to reach neutrality. Subsequently, re-adsorption experiments were employed under identical conditions to explore the performance changes of materials after multiple adsorption–desorption cycles.

The concentrations of TC were determined with a UV-2600 spectrophotometer (Shimadzu, Japan) at 357 nm. The removal efficiency (R, %) and adsorption performance at time (Q_t, $mg{\cdot}g^{-1}$) were based on eqs 5 and 6, respectively:

$$R = \frac{(C_0 - C_t)}{C_0} \times 100\% \quad (5)$$

$$Q_t = \frac{(C_0 - C_t) \times V}{m} \quad (6)$$

where C_0 and C_t represent the initial and remaining concentrations of TC during adsorption, respectively. V represents the TC solution volume (mL), and m is the mass of the adsorbent (mg).

2.7. Model Fitting

The pseudo-first-order and pseudo-second-order kinetic models were studied to explore the adsorption mechanisms of TC, as described by eqs 7 and 8:

$$\ln(Q_e - Q_t) = \ln Q_t - k_1 t \quad (7)$$

$$\frac{t}{Q_t} = \frac{1}{k_2 Q_e} + \frac{t}{Q_e} \quad (8)$$

where t represents the adsorption time, k_1 denotes the rate constant of the pseudo-first-order kinetic model (min^{-1}), and k_2 indicates the rate constant of the pseudo-second-order kinetic model ($g{\cdot}mg^{-1}{\cdot}min^{-1}$). Q_e represents the adsorption performance at equilibrium ($mg{\cdot}g^{-1}$).

Langmuir and Freundlich were also used to fit the adsorption isotherms based on eqs 9 and 10:

$$\frac{1}{Q_e} = \frac{1}{C_e Q_m K_L} + \frac{1}{Q_m} \quad (9)$$

$$\ln Q_e = \frac{1}{n} \ln C_e + \ln K_F \quad (10)$$

where K_L and K_F denote the Langmuir constant ($L{\cdot}mg^{-1}$) and the Freundlich constant [($mg{\cdot}g^{-1}$) ($L{\cdot}mg^{-1}$)], respectively. Q_m denotes the maximum adsorption capacity at equilibrium. n denotes the adsorption intensity.

3. RESULTS AND DISCUSSION

3.1. Delignification Efficiencies and Compositions

The extraction efficiency and chemical compositions of the samples are summarized in Figure 1a,b. The results highlight the effectiveness of the ChCl/MA/GVL ternary DES for delignification: untreated sunflower stalks contain 35.32% cellulose, 10.36% hemicellulose, and 25.9% lignin, which is consistent with the literature.[50] During the ternary DES pretreatment, the efficient release of H^+ from DES facilitates the cleavage of β–O–4 ether linkages and hydrogen bonds within lignin–carbohydrate complexes (LCCs), thereby promoting the effective fractionation of the components (i.e.,

https://doi.org/10.1021/acssusresmgt.6c00244
ACS Sustainable Resour. Manage. XXXX, XXX, XXX–XXX

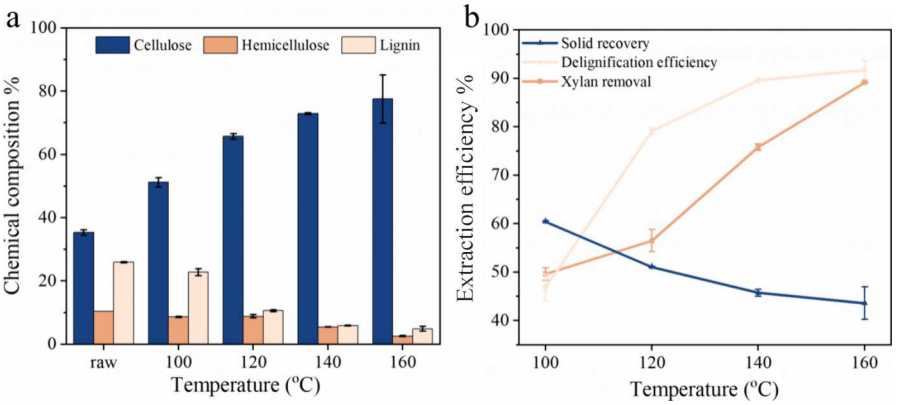

Figure 1. (a) Compositions of raw materials and samples treated with various temperatures. (b). Solid recovery, hemicellulose (xylan) removal, and delignification efficiency.

lignin, cellulose, and hemicellulose),[51] and the content of lignin and hemicellulose in the sunflower stalks exhibits a declining trend, decreasing from 25.9 to 4.90% and from 10.36 to 2.58%, respectively. As the processing temperature increases, cellulose content rises from 35.32 to 77.55% due to the diminution of lignin and hemicellulose. Specifically, high temperatures enhance proton reactivity, thus promoting the crack of β–O–4 bonds of lignin and disrupting the hydrogen/ether bonds between polysaccharides and lignin. This depolymerization was further evidenced by GPC analysis of the dissolved lignin obtained from various temperatures. (ESI Table S1), which showed a decrease in the average molecular weight (3184–2458 g·mol^{-1}). Meanwhile, the reduced viscosity of the ternary DES at elevated temperatures improves molecular contact between the lignocellulosic matrix and the ternary DES, thereby enhancing permeability and lignin extraction efficiency. The sample treated at 160 °C achieved the highest lignin removal rate of 91.70%, which is higher than the delignification rate (31.47 to 62.03%) of the maleic acid/choline chloride/ethylene glycol ternary DES system from Han's report, demonstrating the efficiency of the ChCl/MA/GVL ternary DES system.[52] Pretreatment temperature is an important factor affecting lignin extraction by DES. However, the delignification efficiencies at 140 and 160 °C are comparable (89.63 vs 91.70%), indicating that further increasing the temperature did not significantly enhance lignin removal. This suggests that excessively high temperatures are not necessarily required during the pretreatment process. Particularly in practical industrial applications, lower-temperature operation is advantageous not only for reducing energy consumption but also for improving process safety. Consequently, 140 °C is identified as the optimal temperature for ChCl/MA/GVL ternary DES pretreatment, achieving 75.80% hemicellulose removal and 89.63% lignin removal. The solid recovery of the samples obtained from various temperatures are presented in Figure 1b. A negative correlation is observed between the temperature (100–160 °C) and the yield, which range from 60.44 to 43.60%, suggesting that the removal efficiency of lignin and hemicellulose was significantly improved at higher DES temperatures. Overall, as temperature is widely recognized as one of the most critical factors governing DES delignification efficiency and the subsequent fibrillation performance of LCNFs, based on preliminary exploratory experiments and the scope of this study, it was selected as the main variable to investigate its effect on biomass fractionation and to demonstrate the feasibility of the DES/GV ternary DES system for efficient LCNF preparation. Other operational parameters, including treatment time, DES composition, biomass-to-solvent ratio, and solid loading, were not investigated in this study; however, they also play important roles in biomass fractionation. Therefore, multivariate optimization will be an important topic in our future work.

3.1.1. FT-IR Analysis. FT-IR was performed to detect the functional group changes during DES processing (Figure 2a). The absorption bands observed at 3326 cm^{-1} are consistent with O–H stretching vibrations, and their intensity increases with higher processing temperatures. This observation indicates that DES processing facilitates the exposure of hydroxyl groups in cellulose, likely owing to the breaking of hydrogen bond and the removal of lignin and hemicellulose. The C–H vibration at approximately 2881 cm^{-1} is attributed to the alkyl chains of cellulose/hemicellulose. The signals at 1724 cm^{-1} are the carbonyl vibrations from esters, suggesting the possible occurrence of esterification reactions between the carboxylic acid groups in the DES and the hydroxyl groups of cellulose during the pretreatment process.[53] The bands at 1605 and 1514 cm^{-1} are associated with the C═C stretching vibrations, which is due to the presence of lignin.[54] These two bands exhibit a decrease in intensity with increasing temperature, implying the progressive removal of lignin from the cellulose matrix during DES pretreatment. The absorption peak at 1244 cm^{-1} is only observed in untreated biomass and gradually disappears with increasing temperature, likely associated with the cleavage of ester linkages between lignin and hemicellulose[55]. The peaks at 1033 cm^{-1} are related to the stretching vibrations of C–O–C bonds in cellulose rings. The absorption peaks near 897 cm^{-1} refer to the asymmetric out-of-plane stretching caused by the β-glycosidic bonds between glucose units, which confirms that the cellulose structure remains intact. According to the FT-IR analysis, no significant evidence of residual DES-derived compounds was observed in the obtained LCNFs, and the slight enhancement in the intensity of these peaks suggests a *purer* cellulose spectrum after ternary DES treatment. Overall, the disappearance of bands corresponding to noncellulosic components proves the capability of DES treatment, and cellulose became the dominant remaining component.

3.1.2. NMR. To further investigate the chemical structure changes of LCNFs following treatment with various temperatures, stacked ^{13}C CPMAS spectra were employed and shown

https://doi.org/10.1021/acssusresmgt.6c00244
ACS Sustainable Resour. Manage. XXXX, XXX, XXX–XXX

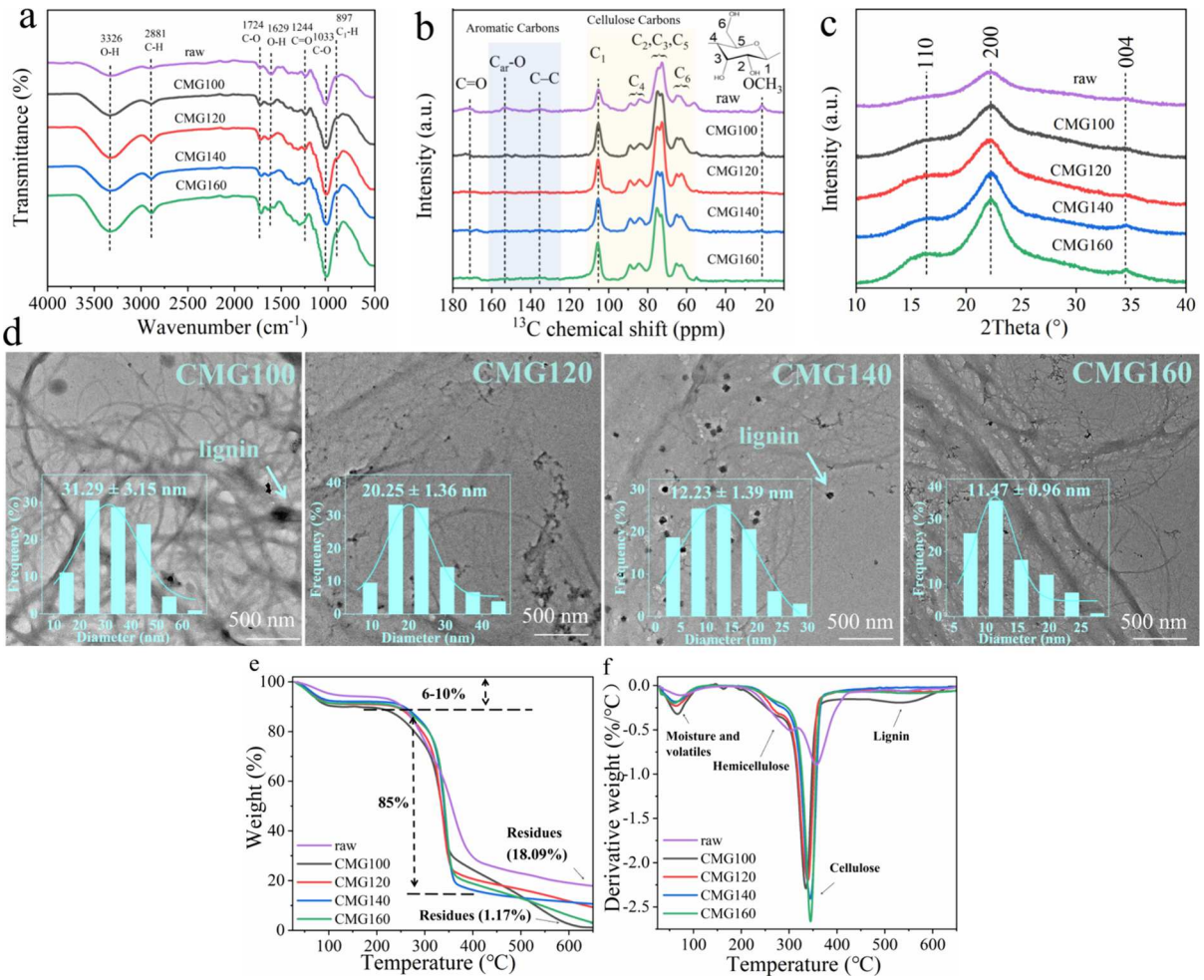

Figure 2. (a) FT-IR profiles, (b) ^{13}C NMR spectra, and (c) XRD pattern of samples obtained from various temperatures. (d) TEM images and fibril dimension distributions of LCNFs obtained from CMG100, CMG120, CMG140 and CMG160. (e) TGA thermograms and (f) DTG profiles.

in Figure 2b. The resonances at approximately 175 ppm correspond to the carbonyl and carboxylic groups in hemicelluloses present in the sunflower stalk plant cell wall, while the signals at 153 and 135 ppm are indicative of carbonyl/carboxylic groups and oxygenated aromatic carbons in lignin, respectively.[56] The peaks at 55.86 ppm originate from the methoxy groups of lignin, and the signals at 21.3 ppm are attributed to the acetyl group of hemicellulose. After treatment, the disappearance of these peaks with respect to increasing temperatures indicates the successful removal of lignin and hemicellulose, further corroborating the FT-IR results. Notably, the samples exhibit characteristic cellulose carbons (C_1 to C_6) ranging from 110 to 60 ppm.[57] With increasing pretreatment temperature, the increased intensity of C_1 carbons suggests a higher cellulose content in the residual samples. Additionally, the changes of cellulose structure are further observed: the ratio of amorphous carbons of cellulose at C_4 and C_6 (83 and 62 ppm) starts to reduce, while the ratio of crystalline carbons at C_4 and C_6 (88 and 64 ppm) begins to increase. This indicates that the amorphous cellulose was also removed during the treatment process, alongside lignin and hemicellulose,[58] corroborating the results obtained from X-ray diffraction. The CrI of raw materials and LCNFs were calculated as 31.85, 39.68, 44.25, 44.64, and 45.66% as the treatment temperature increased, owing to the removal of disordered lignin and polysaccharide. In summary, ternary DES treatment effectively separates lignin and hemicellulose, allowing cellulose to remain intact while increasing its crystalline character.[59]

3.1.3. X-ray Powder Diffraction. XRD was employed to evaluate the crystalline structure of the samples, with patterns displayed in Figure 2c. Characteristic peaks for crystalline cellulose were observed at 2θ values of 16.4°, 22.2°, and 34.5°, corresponding to the Miller indices (110), (200), and (004) crystallographic planes, respectively.[60] This indicates that cellulose I is the predominant crystalline form in the samples, and as the temperature of DES treatment increases from 100 to 160 °C, the peaks at 16.4°, 22.2°, and 34.5° become more pronounced, suggesting the gradual dissolution of amorphous cellulose and hemicellulose, along with lignin, thereby an enhancement in the crystallinity of the samples is observed (the crystallinity index ranging from 39.68 to 45.66%, as calculated by ^{13}C NMR spectra). These results demonstrate that the CrI of the samples is positively associated with temperature, and higher DES pretreatment temperatures can effectively enhance proton reactivity and promote the selective cleavage of covalent linkages and hydrogen-bonding networks between the lignin–polysaccharide complex, thus altering the crystallinity of cellulose without disrupting its crystal structure.

https://doi.org/10.1021/acssusresmgt.6c00244
ACS Sustainable Resour. Manage. XXXX, XXX, XXX–XXX

3.1.4. Morphology of LCNFs. The morphology of LCNFs and their fibril dimensions were defined by TEM and shown in Figure 2d. All samples present nanoscale dimensions with good dispersibility, suggesting successful DES and homogenization pretreatment for noncellulosic removal and nanofiber production from biomass. Additionally, the hydrogen bond linkages within the cellulose structure were also disrupted, leading to the cracking of the structures into fine nanofibers. All samples exhibit a decreasing trend in average widths of nanofibrils from 31.29 to 11.47 nm as the reaction temperature increased from 100 to 160 °C, likely owing to the diminution of intermolecular hydrogen bonds, and the viscosity of the DES reduces at higher temperatures, facilitating the diffusion of molecules into the lignocellulosic structure and allowing them to compete for hydrogen bonds. This leads to a higher degree of cellulose depolymerization and reduced diameters of LCNFs.[30] Irregularly sized dark particles observed in the images are likely residual lignin that was not entirely removed during treatment.[61] Overall, the LCNFs demonstrated good dispersibility with small diameters, which is favorable for further valorization, especially for reinforcing agents.

3.1.5. Zeta Potential. To access the colloidal stability of nanoparticle suspensions, the zeta potential of the LCNFs were analyzed and shown in Table 1. The abundance of hydroxyl groups on LCNFs results in a negative zeta potential value in aqueous suspensions, with surface charge falling from −19.71 to −27.49 mV as temperatures increase from 100 to 160 °C, suggesting the good stability of LCNF suspensions prepared through DES pretreatment. Notably, higher temperatures facilitate the exposure of more hydroxyl and carboxyl groups, consistently leading to a more negative zeta potential, which enhances the stability of the LCNF system. This also aligns with the intensity of FT-IR spectra (O–H and carbonyl vibrations at 3326 and 1724 cm^{-1}, respectively), demonstrating the effective regulation of temperature on the colloidal behavior of LCNFs.

3.1.6. Thermal Stability Analysis of LCNFs. Thermogravimetric (TG) and derivative thermogravimetric (DTG) analyses of raw biomass and LCNFs are performed and illustrated in Figure 2e,f. The raw materials exhibit a higher residue content than LCNFs (approximately 18.09% compared to 1.17%), likely due to the removal of lignin and inorganic minerals (e.g., potassium, phosphorus, aluminum, and iron) during DES treatment.[62] Notably, the extremely low residual content of samples confirms the high delignification efficiency in the DES/GVL system. Three primary degradation stages are observed from the DTG: (1) The weight loss (6–10 wt %) observed between 30 and 120 °C is attributed to volatile compounds and moisture. (2) The most obvious mass loss (approximately 85%) occurs in the second stage between 180 and 420 °C, mainly owing to polysaccharide (e.g., hemicellulose and cellulose) degradation. Notably, a small peak (ranging from 250 to 280 °C) associated with hemicellulose at the front shoulder of the main peaks begins to diminish. This suggests the gradual removal of hemicellulose with increasing processing temperature, consistent with changes in chemical composition. Additionally, the main peaks ranging from 300 to 400 °C are associated with cellulose, and the decomposition temperature shifts to the right with increasing pretreatment temperature, likely due to the removal of noncrystalline cellulose, resulting in highly compact crystalline LCNFs and enhancing their thermal stability,[63] as confirmed by NMR results. However, the raw sample exhibits the highest decomposition temperature (356 °C) compared to the samples treated with DES, likely owing to the cracking of hydrogen bond network of cellulose during DES treatment, thereby reducing its thermal stability. (3) The third stage, occurring after 400 °C, is attributed to the degradation and carbonization of lignin,[64] with no obvious bands observed after treatment, indicating the high delignification efficiency of the novel ternary DES/GVL solvents.

Table 1. Zeta Potential of LCNFs (mV) Obtained from Various Temperatures

Temperature (°C)	Zeta potential (mV)
100	−19.71 ± 0.79
120	−22.47 ± 0.06
140	−23.69 ± 1.58
160	−27.49 ± 0.57

3.2. Hydrogel Composite

3.2.1. FT-IR Spectra. The FT-IR spectra of SA, PAM, LCNF, and hydrogel composite are presented in Figure 3a,b. SA exhibit similar chemical structures to cellulose: the absorbance band at 3259 cm^{-1} represents the O–H stretching vibration, and C–O vibrations are observed at 1593, 1405, and 1025 cm^{-1}, respectively. For AM, the bands at 3329 and 3163 cm^{-1} are related to the symmetric and asymmetric N–H vibrations, respectively. The band of the C═O stretching vibration is detected at 1658 cm^{-1}, while the signal at 1604 cm^{-1} is due to the C═C double bond stretching vibrations. Additionally, the band at 1419 cm^{-1} corresponds to the C–N stretching vibrations of the amide group.[65] Detailed characterization of LCNFs is provided in section 3.1.1. When compared to the individual material, the N–H stretching vibration absorption in both PAM/SA and PAM/SA/LCNF hydrogels becomes significantly broader, indicating enhanced intermolecular hydrogen bonding between the constituent materials. The disappearance of C═C functional group at 1604 cm^{-1} in the synthesized hydrogels confirms the successful polymerization of AM to form PAM. Notably, the C–O symmetric vibration signals shift from 1593 cm^{-1} in SA and 1639 cm^{-1} in LCNF to 1610 cm^{-1} in both PAM/SA and PAM/SA/LCNF hydrogels, suggesting that the presence of Al^{3+} ions in the composite hydrogels induces a more compact structure.[66]

3.2.2. XRD Analysis. The XRD patterns of LCNF, PAM/SA, and PAM/SA/LCNF hydrogels are depicted in Figure 3c. Detailed characterization of LCNFs is provided previously in section 3.1.3. The PAM/SA/LCNF hydrogel exhibits a broad peak around 25.7°, indicative of an amorphous structure dominating the hydrogel matrix. A small peak at 22.4° in the PAM/SA/LCNF hydrogel corresponds to a characteristic peak of LCNFs, confirming successful compounding of PAM/SA and LCNF through hydrogen bonding and physical entanglement. Compared to the PAM/SA composite, the PAM/SA/LCNF composite demonstrates relatively stronger diffraction intensity, which may be attributed to the cross-linking between LCNF and PAM/SA, thereby enhancing crystallinity within the hydrogel.[67]

3.2.3. SEM Analysis of Hydrogels. The microstructural features of the hydrogel composites were systematically analyzed by SEM, which are shown in Figure 3d,e. Both hydrogels exhibit typical 3D hierarchical porous structures; this characteristic represents the typical networked porous structure of hydrogel materials. Notably, the PAM/SA/LCNF hydrogels

https://doi.org/10.1021/acssusresmgt.6c00244
ACS Sustainable Resour. Manage. XXXX, XXX, XXX−XXX

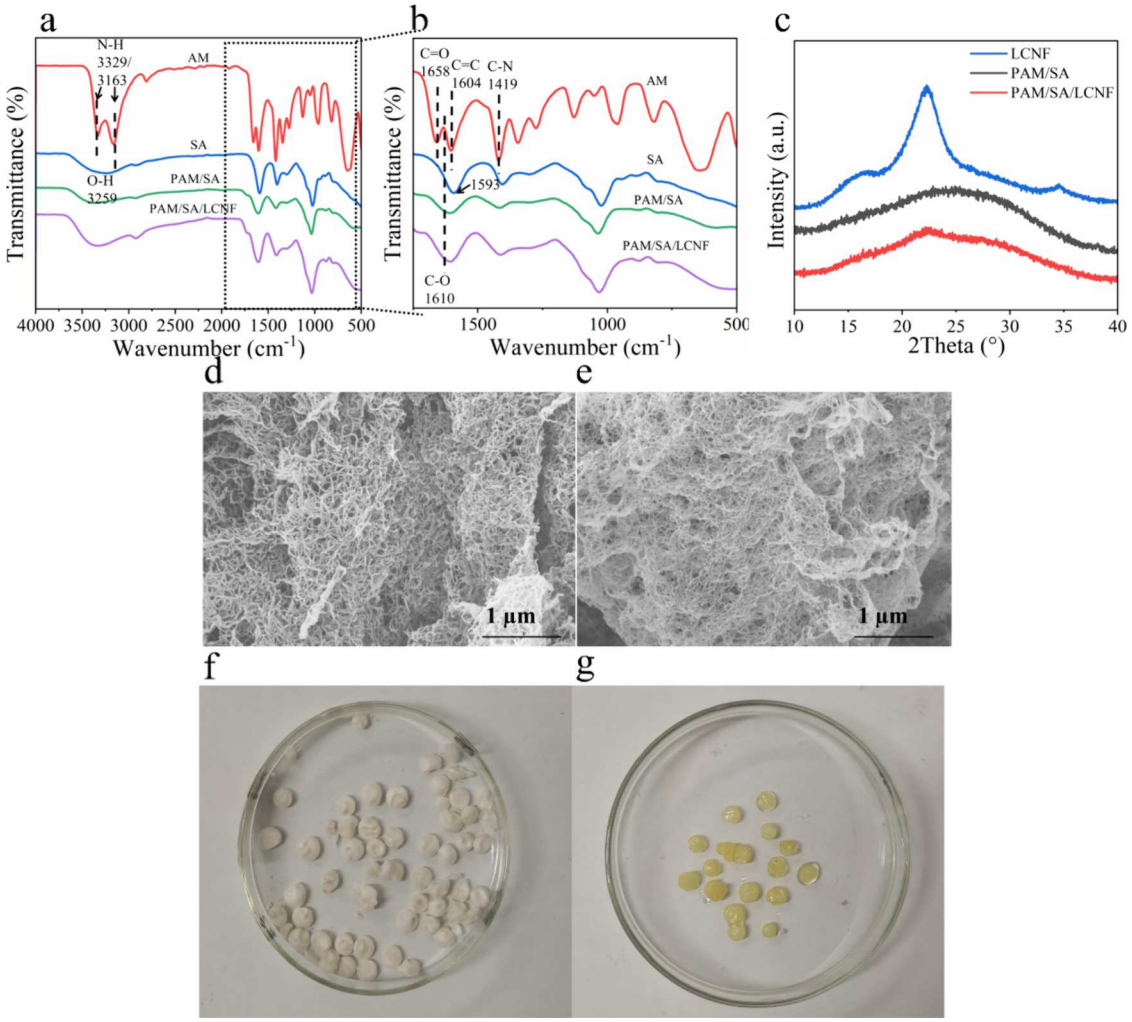

Figure 3. (a) FT-IR and (b) expanded FT-IR spectra of hydrogels. (c) XRD diffractograms of hydrogels. (d) TEM images of PAM/SA and (e) PAM/SA/LCNF hydrogels. Appearance of the PAM/SA/LCNF hydrogel (f) before and (g) after adsorption.

display a denser interpenetrating network structure, attributed to the incorporation of LCNF, which forms a tightly connected and irregular pore network with PAM/SA through strong hydrogen bonding, thereby enhancing intermolecular interactions. This porous network structure provides favorable conditions for subsequent tetracycline adsorption (Figure 3f,g).

3.2.4. Univariate Adsorption Assays. The determination of optimal adsorbent dosage is a critical parameter in wastewater treatment processes, as it significantly influences pollutant removal efficiency while controlling treatment costs. As shown in Figure 4a, increasing the hydrogel adsorbent dosage (5–25 mg) rapidly enhances the removal efficiency of tetracycline (TC) from 59.05 to 90.99%. This improvement is owing to the increased adsorption area and active sites, which promote pollutant adsorption. However, a decrease in adsorption capacity per unit mass is observed from 141.70 to 43.68 mg·g^{-1} with increasing adsorbent amount, which may be due to the available active sites being effectively utilized at lower adsorbent dosages, resulting in a higher adsorption capacity. However, the adsorption process tends to reach equilibrium more quickly at higher dosages; even though more active sites are available, the presence of osmotic pressure limits the accessibility of reaction sites. Consequently, the inefficient utilization of these sites leads to a reduced overall adsorption capacity.[68] Thus, when the dosage is below 10 mg, the adsorption performance rises significantly, but the removal rate drops sharply. Conversely, the adsorption capacity gradually decreases while the removal rate continues to increase when the amount of adsorbent exceeds 10 mg. Considering both removal efficiency and adsorption capacity, an adsorbent dosage of 15 mg was selected for subsequent systematic investigations into additional governing factors affecting adsorption efficacy.

Figure 4b illustrates the effect of different adsorption times on the removal rate and adsorption performance of TC. The values of the PAM/SA/LCNF hydrogel rapidly reach 80.45% (removal efficiency) and 64.36 mg·g^{-1} (adsorption capacity), respectively, within 10–210 min. Subsequently, during the intermediate stage (210–600 min), both adsorption capacity (71.18 mg·g^{-1}) and removal rate (88.98%) continue to increase, although at a reduced rate. In the final stage (600–1440 min), the adsorption performance stabilizes, with the adsorption capacity and removal rate reaching plateaus of 73.84 mg·g^{-1} and 92.3%, respectively. Relative to advanced adsorbents, e.g., MOFs (69.42%),[69] COFs (81.2%),[70] and carbon-based

https://doi.org/10.1021/acssusresmgt.6c00244
ACS Sustainable Resour. Manage. XXXX, XXX, XXX–XXX

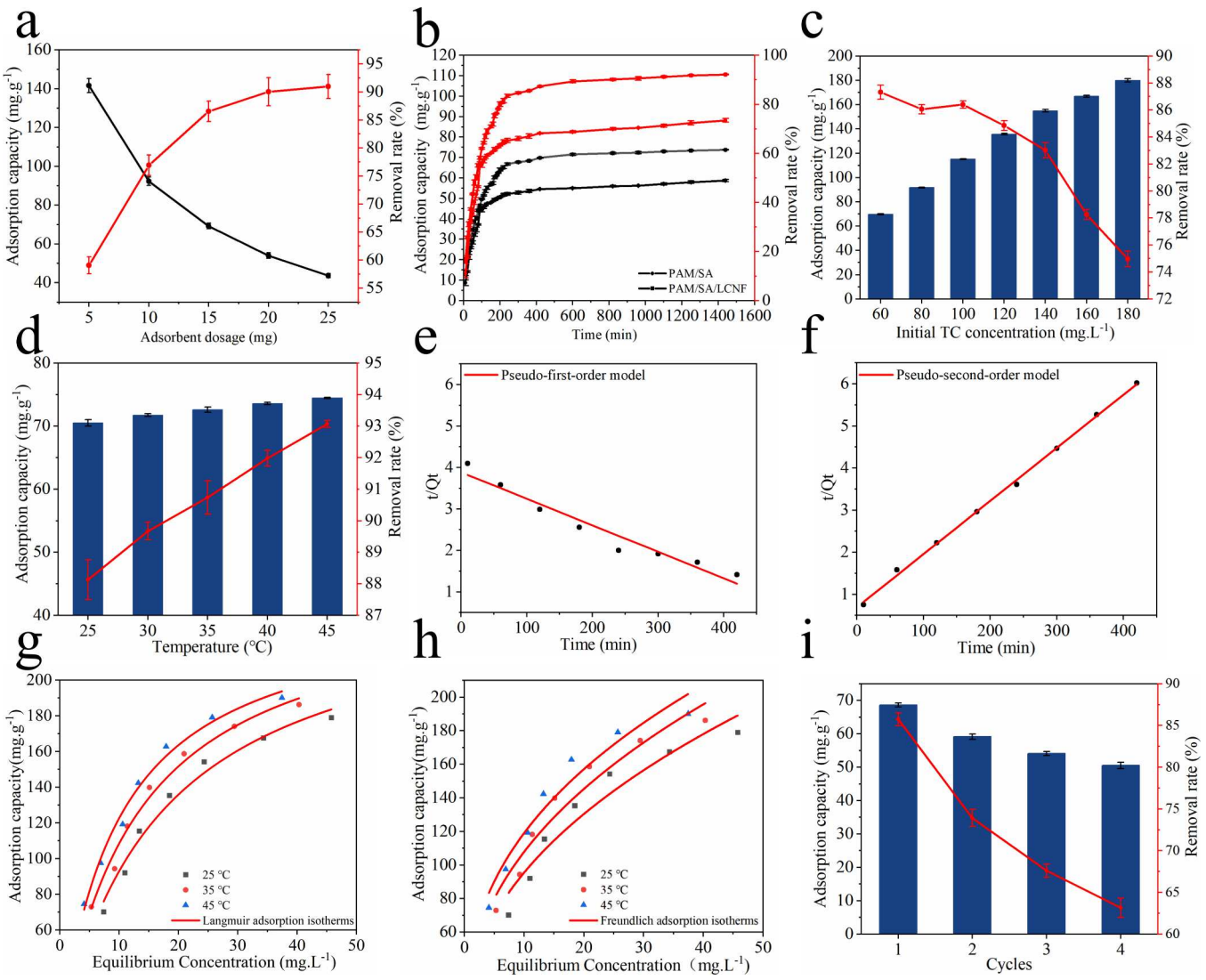

Figure 4. Impact of (a) dosage, (b) adsorption time, (c) initial TC concentration, and (d) temperature on TC adsorption performance. Fitted curves of (e) pseudo-first-order and (f) pseudo-second-order kinetic of TC. (g) Langmuir and (h) Freundlich fitting curves for TC adsorption at different temperatures. (i) Regeneration and reusability of the hydrogel.

materials (85.04%),[71] it demonstrates specific advantages over its counterparts. Even compared with similar materials (e.g., cellulose/alginate-based adsorbents), it has a better removal effect, and the results are displayed in Table 2. This is owing to the kinetic progression of adsorption: abundant available adsorption sites enable rapid uptake of TC during the initial stage. However, as adsorption time progresses, accessible sites progressively diminish, leading to a decline in adsorption rate. In the later phase, TC molecules migrate and diffuse into the adsorbent's interior matrix, ultimately reaching an equilibrium state characterized by stabilized adsorption capacity and removal efficiency. The PAM/SA hydrogel exhibits similar trends, but the adsorption capacity and removal rate were significantly superior to those of PAM/SA hydrogels under identical conditions (58.37 $mg{\cdot}g^{-1}$ and 72.96%). This improvement may be because the DES treatment successfully introduced a high density of carboxylic (–COOH) and hydroxyl (–OH) groups onto the LCNF surface (see section 3.1.1), which provides abundant active sites for electrostatic attraction and hydrogen bonding to the TC. Simultaneously, a significant increase in the specific surface area was achieved (see section 3.2.3), a feature that enlarges the interface for mass transfer. This synergistic combination of enriched surface chemistry and enlarged accessible area directly accounts for the observed enhancement in the adsorption properties,[72]

Table 2. Comparison of the Maximum Adsorption Capacities of PAM/SA/LCNF with respect to other matrices and CEL/Alg for TC Removal

	Q_m ($mg{\cdot}g^{-1}$)	Removal rate (%)	Conditions	Reusability	ref
PAM/SA/LCNF	73.84	92.30	TC concentration was 60 $mg{\cdot}L^{-1}$	49.87 $mg{\cdot}g^{-1}$ after four cycles	this paper
CEL/Alg	28.21	85.78	TC concentration was 10 ppm, pH = 7		73
Cu-immobilized alginate adsorbent	53.26		TC concentration was 60 $mg{\cdot}L^{-1}$ pH = 3	10.32 $mg{\cdot}g^{-1}$ after five cycles	74
PAM/CA@Cu	≈50		TC concentration was 50 $mg{\cdot}L^{-1}$ pH = 5	<45 $mg{\cdot}g^{-1}$ after three cycles	75

https://doi.org/10.1021/acssusresmgt.6c00244
ACS Sustainable Resour. Manage. XXXX, XXX, XXX–XXX

indicating the adsorption enhancement effect conferred by LCNF incorporation. According to the adsorption performance for TC and experimental results, a reaction time of 600 min was chosen for further experiments.

The influence of initial TC concentration was investigated and shown in Figure 4c. An increase in concentration from 60 to 180 mg·L^{-1} results in a reduction of the removal rate from 87.69 to 74.57%. This reduction is due to fewer available adsorption sites at higher initial concentrations, thereby lowering the removal rate. However, the adsorption capacity of the hydrogel increases from 70.15 to 178.79 mg·g^{-1} over the same concentration range, indicating that higher initial concentrations significantly enhance TC adsorption. This phenomenon is attributed to enhanced mass transfer and adsorption kinetics of TC molecules at higher concentrations, making it easier for TC to enter the internal voids of the hydrogel. The higher concentration results in more TC molecules per unit volume, leading to increased contact with hydrogel and consequently higher adsorption capacity.

Figure 4d illustrates the influence of temperature on the composite for TC adsorption. The adsorption performance of the hydrogel gradually increases from 70.15 to 74.52 mg·g^{-1} with increasing temperature from 25 to 45 °C. Concurrently, the removal rate exhibits an increasing trend from 87.69 to 93.14%. This trend indicates that higher temperatures accelerate molecular motion and improve mass transfer and intramolecular diffusion rates of TC in the liquid phase, facilitating the entry of TC into the hydrogel's internal pore structure and thereby improving adsorption performance.

Table 3. Adsorption Isotherm Parameters of TC Based on Langmuir and Freundlich Models at Various Temperatures

Model	Parameter	25 °C	35 °C	45 °C
Langmuir	Q_{max} (mg·g^{-1})	252.39	252.30	245.63
	K_L	0.0583	0.0753	0.0996
	R^2	0.981	0.986	0.989
Freundlich	K_F	33.943	40.099	47.430
	n	2.23	2.33	2.50
	R^2	0.937	0.948	0.953

Although the hydrogel demonstrated promising adsorption performance under laboratory batch conditions, several issues remain to be addressed before industrial implementation, including relatively long equilibrium times, possible mass transfer limitations, competitive adsorption effects in complex wastewater matrices, and swelling-related issues under continuous-flow conditions. Therefore, the present work is primarily intended to demonstrate the feasibility of utilizing DES-derived lignocellulosic nanofibres as sustainable hydrogel components for tetracycline adsorption. Future studies will focus on optimizing adsorption kinetics and evaluating the material under dynamic continuous-flow conditions and realistic wastewater environments.

3.2.5. Adsorption Kinetics and Thermodynamic Analysis. To investigate the adsorption rates and identify potential rate-controlling steps, adsorption kinetics were analyzed and shown in Figure 4e,f. A higher correlation coefficient is observed for the pseudo-second-order model (R^2 = 0.998) compared to the pseudo-first-order model (R^2 = 0.949), indicating superior fitting performance. Meanwhile, the data from the pseudo-second-order model (Q_e= 79.24 mg·g^{-1}) is closer to the experimentally obtained value (Q = 69.71 mg·g^{-1}) than the prediction from the pseudo-first-order model. This indicates that the pseudo-second-order model better represents the adsorption behavior of the hydrogel toward TC removal, suggesting that this process is mainly governed by chemical adsorption. Although numerous adsorbents for tetracycline have been reported with adsorption capacities [e.g., ZIF-8 nanoparticles (90 mg·g^{-1}),[76] hydrochar (75.47 mg·g^{-1}),[77] and magnetic chitosan-based microspheres (92 mg·g^{-1})][78] and are comparable to that of our material, the hydrogel developed in this study remains highly competitive considering its cost-effectiveness and ease of preparation.

To explore the adsorbate–adsorbent interactions, the adsorption isotherms of TC on the hydrogel were studied from 25 to 45 °C. With increasing temperature, the adsorption performance of the hydrogel increases and eventually stabilizes. Both the Langmuir (Figure 4g) and Freundlich (Figure 4h) models were applied to analyze the interactions at the adsorbate-adsorbent interface, which is shown in Table 3. The correlation coefficients (R^2) of the Langmuir model (0.981,

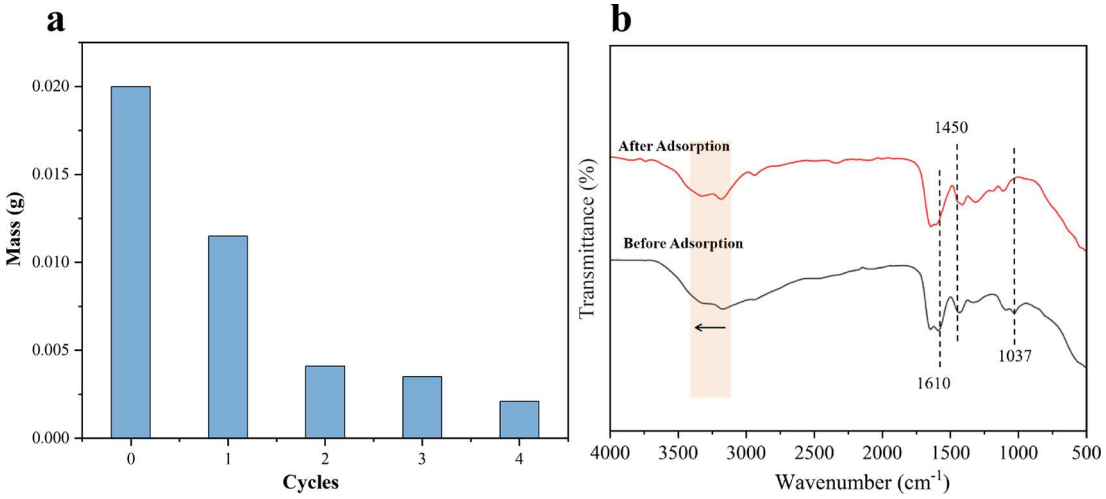

Figure 5. (a) Hydrogel mass loss after four cycles. (b) FT-IR spectra of hydrogels before and after TC adsorption.

https://doi.org/10.1021/acssusresmgt.6c00244
ACS Sustainable Resour. Manage. XXXX, XXX, XXX–XXX

0.986, and 0.989) are higher than the Freundlich model (0.937, 0.948, and 0.953) from 25 to 45 °C. This indicates that the adsorption of TC onto the hydrogel follows a monolayer adsorption process, with adsorption sites uniformly distributed on the hydrogel surface, as observed in the SEM images. The Langmuir model fitting results (178.96, 186.22, and 190.07 $mg{\cdot}g^{-1}$) are also close to the maximum adsorption values of 252.39, 252.30, and 245.63 $mg{\cdot}g^{-1}$. Finally, the Freundlich constants (n) in Table 2 are 2.23, 2.33, and 2.50, which fall within the range of 2–10, suggesting that the adsorption behavior is thermodynamically favorable.

3.2.6. Hydrogel Regeneration and Reusability. The separation efficiency and recyclability of the adsorbent are crucial for its practical application. To assess these properties, the regeneration and reusability of the hydrogel were systematically evaluated, and the adsorption performance over four adsorption–desorption cycles is presented in Figure 4i.

Compared with the initial adsorption performance of 73.84 $mg{\cdot}g^{-1}$, with increasing cycle number, the values decrease from 68.17 to 49.87 $mg{\cdot}g^{-1}$, while the removal rate declines from 85.21 to 62.34%. The reduction in adsorption performance can therefore be attributed to the partial occupation of active sites. To better understand the chemical changes before and after tetracycline adsorption, the FT-IR spectra were recorded, as shown in Figure 5b. The characteristic absorbance bands at 1610 and 1037 cm^{-1} are attributed to the vibrations of carboxyl and hydroxyl groups, respectively. The intensity of these bands lessened after the recycling process, indicating a decrease in the accessible active sites available for TC adsorption. After adsorption, the appearance of a new characteristic vibrational band at approximately 1450 cm^{-1} associated with aromatic C–H bending clearly indicates the presence of TC on the hydrogel surface, confirming the successful capture of TC molecules. The broad –OH stretching band shifted to a higher wavenumber, suggesting the formation of intermolecular hydrogen bonds between TC and the abundant surface of materials. These interactions are expected to facilitate the efficient adsorption of TC. Meanwhile, the progressive structural degradation and significant material loss of the hydrogel matrix during repeated cycling processes, evidenced by the decrease in adsorbent mass from 0.0200 to 0.0021 g (Figure 5a), also contributed to the deterioration of the adsorption performance. Despite this, Liao et al. reported that the adsorption loss rate of PVA-CA gel beads for TC after four cycles was 23.59%.[79] Our results still show a relatively high adsorption capacity (49.87 $mg{\cdot}g^{-1}$) and removal rate (62.34%) for TC, indicating the material's promising potential for tetracycline removal from wastewater.

4. CONCLUSIONS

A ternary DES comprising ChCl, MA, and GVL was evaluated to produce LCNFs from sunflower stalks, and the LCNFs were then combined with PAM and SA to remove TC from wastewater. The ternary DES system achieved high removal efficiencies: 89.17% for hemicellulose and 91.70% for lignin. The resulting LCNFs exhibited improved properties with higher pretreatment temperatures. Specifically, crystallinity increased from 31.85 to 45.66%, thermal stability rose from 335 to 345 °C, and the zeta potential shifted from −19.71 to −27.49 mV. Subsequently, PAM/SA/LCNF hydrogels with a porous network structure were successfully prepared. These hydrogels demonstrated enhanced TC adsorption performance (92.3%), attributed to LCNF incorporation. The results demonstrate the significant effectiveness and promise of the ternary DES/GVL system for LCNF production and confirm LCNFs as an effective, eco-friendly adsorbent for TC removal from water.

■ ASSOCIATED CONTENT

Supporting Information

The Supporting Information is available free of charge at https://pubs.acs.org/doi/10.1021/acssusresmgt.6c00244.

Chemical composition and structure analysis of LCNFs (1.1), schematic diagram of PAM/SA/LCNF hydrogel preparation (Figure S1), and determination of LNP molecular weight and polydispersity (Table S1) (DOCX)

■ AUTHOR INFORMATION

Corresponding Authors

Yang Gao – *State Key Laboratory of Separation Membrane and Membrane Process, School of Chemistry, Tiangong University, Tianjin 300387, PR China;* orcid.org/0000-0001-8233-7747; Email: yg1042@tiangong.edu.cn

Shichao Xu – *School of Environmental Science and Engineering, Tiangong University, Tianjin 300387, PR China;* orcid.org/0000-0002-9488-565X; Email: xushichao@tiangong.edu.cn

Avtar S. Matharu – *Green Chemistry Centre of Excellence, Department of Chemistry, University of York, York YO10 5DD, UK;* orcid.org/0000-0002-9488-565X; Email: avtar.matharu@york.ac.uk

Authors

Ruipeng Ji – *State Key Laboratory of Separation Membrane and Membrane Process, School of Chemistry, Tiangong University, Tianjin 300387, PR China;* orcid.org/0009-0000-8795-7152

Ziyi Ren – *State Key Laboratory of Separation Membrane and Membrane Process, School of Chemistry, Tiangong University, Tianjin 300387, PR China*

Zhicheng Jiang – *College of Biomass Science and Engineering, Sichuan University, Chengdu 610065, PR China;* orcid.org/0000-0002-8096-4971

Complete contact information is available at: https://pubs.acs.org/doi/10.1021/acssusresmgt.6c00244

Author Contributions

Yang Gao: writing, conceptualization, original draft, funding acquisition; Ruipeng Ji: data curation; Ziyi Ren: data curation; Zhizheng JIang: figures; Shichao Xu: review & editing; Avtar S. Matharu: initial research and ongoing discussions, review & editing.

Notes

The authors declare no competing financial interest.

■ ACKNOWLEDGMENTS

The work was supported by Faculty Recruitment Funds (5201030128).

REFERENCES

(1) Aslam, B.; Asghar, R.; Muzammil, S.; Shafique, M.; Siddique, A. B.; Khurshid, M.; Ijaz, M.; Rasool, M. H.; Chaudhry, T. H.; Aamir, A. J. G.; et al. AMR and Sustainable Development Goals: at a crossroads. *Global Health* **2024**, *20* (1), No. 73.

(2) Bhattacharya, R.; Bose, D.; Gulia, K.; Jaiswal, A.; Energy, S. Impact of antimicrobial resistance on sustainable development goals and the integrated strategies for meeting environmental and socio-economic targets. *Environ. Prog. Sustainable Energy* **2024**, *43* (1), No. 14320.

(3) Yang, M.; He, J.; He, J.; Cao, J. Devices. Removal of tetracycline and ciprofloxacin from aqueous solutions using magnetic copper ferrite nanoparticles. *J. Sci.: Adv. Mater. Devices* **2024**, *9* (2), No. 100717.

(4) Fu, T.; Wu, S.; Zhao, M.; Zheng, X.; Wang, Z.; Jin, Z.; Fan, C.; Protection, E. Preparation and application of cattail residue-based magnetic cellulose composites for tetracycline antibiotics adsorption. *Process Saf. Environ. Prot.* **2024**, *189*, 598–611.

(5) Gupta, S.; Kaur, R.; Sohal, J. S.; Singh, S. V.; Das, K.; Sharma, M. K.; Singh, J.; Sharma, S.; Dhama, K. Countering zoonotic diseases: current scenario and advances in diagnostics, monitoring, prophylaxis and therapeutic strategies. *Arch. Med. Res.* **2024**, *55* (6), No. 103037.

(6) Liu, J.; Liu, D.; Liu, S.; Li, Z.; Wei, X.; Lin, S.; Guo, M.; Materials, E. Preparation and characterization of sulfated cellulose nanocrystalline and its composite membrane for removal of tetracycline hydrochloride in water. *Energy Environ. Mater.* **2020**, *3* (2), 209–215.

(7) Nguyen, N. T. T.; Phan, A. N. Q.; Van Tran, T.; Nguyen, T. T. T. Morinda citrifolia fruit extract-mediated synthesis of ZnO and Ag/ZnO nanoparticles for photocatalytic degradation of tetracycline. *Environ. Res.* **2025**, *273*, No. 121209.

(8) Sun, J.; Cui, L.; Gao, Y.; He, Y.; Liu, H.; Huang, Z. J. C. P. Environmental application of magnetic cellulose derived from Pennisetum sinese Roxb for efficient tetracycline removal. *Carbohydr. Polym.* **2021**, *251*, No. 117004.

(9) Thanh, L. N.; Wernli, D.; Målqvist, M.; Jørgensen, P. S. 'When global health meets global goals': assessing the alignment between antimicrobial resistance and sustainable development policies in 10 African and Asian countries. *BMJ Global Health* **2025**, *10* (3), No. e017837.

(10) Zango, Z. U.; Ibnaouf, K. H.; Lawal, M. A.; Aldaghri, O.; Wadi, I. A.; Modwi, A.; Zango, M. U.; Adamu, H. Recent trends in catalytic oxidation of tetracycline: An overview on advanced oxidation processes for pharmaceutical wastewater remediation. *J. Environ. Chem. Eng.* **2025** *13*, No. 116979.

(11) Wu, C.-J.; Maggay, I. V.; Chiang, C.-H.; Chen, W.; Chang, Y.; Hu, C.; Venault, A. Removal of tetracycline by a photocatalytic membrane reactor with MIL-53 (Fe)/PVDF mixed-matrix membrane. *Chem. Eng. J.* **2023** *451*, No. 138990.

(12) Ren, H.-T.; Cao, W.-B.; Qin, J.; Cai, C.-C.; Li, D.-S.; Li, T.-T.; Lou, C.-W.; Lin, J.-H. Enhanced removal of tetracycline by sandwich layer composite membrane based on the synergistic effect of photocatalysis and adsorption. *Sep. Purif. Technol.* **2024**, *341*, No. 126910.

(13) Esfandiaribayat, M.; Binazadeh, M.; Sabbaghi, S.; Mohammadi, M.; Ghaedi, S.; Rajabi, H. Tetracycline removal from wastewater via g-C_3N_4 loaded RSM-CCD-optimised hybrid photocatalytic membrane reactor. *Sci. Rep.* **2024**,*14* (1), No. 1163.

(14) Wu, S.; Hu, H.; Lin, Y.; Zhang, J.; Hu, Y. H. Visible light photocatalytic degradation of tetracycline over TiO_2. *Chem. Eng. J.* **2020** *382*, No. 122842.

(15) Li, S.; Hu, J. Photolytic and photocatalytic degradation of tetracycline: Effect of humic acid on degradation kinetics and mechanisms. *J. Hazard. Mater.* **2016**, *318*, 134–144.

(16) Al-Anazi, A.; Al-Hajji, L.; Ismail, A. A.; El-Toni, A. M.; Khan, A.; Han, C. Visible-light-induced mesoporous ZnO hexagonal sheets decorated by $CuAl_2O_4$ nanoparticles for accelerating removal of tetracycline. *Ceram. Int.* **2025**, *51* (11), 14092–14100.

(17) García-Criado, N.; Martín-Pozo, L.; Martín, J.; Santos, J. L.; Aparicio, I.; Alonso, E. Efficient Removal of Tetracyclines and Their Metabolites from Wastewater Using Purified Stevensite: Adsorption Capacity, Reusability, and Antibiotic Decontamination. *Antibiotics* **2025**, *14* (4), No. 395.

(18) Dawood, I.; Zyoud, A. H.; Zyoud, S.; Amireh, A.; Zyoud, S. H.; Kim, T. W. Sustainable water purification through the adsorptive removal of tetracycline via modified clay and regeneration via controlled thermolysis: a reusable and environmentally friendly approach for contaminant mitigation. *Appl. Water Sci.* **2025**, *15* (8), 1–26.

(19) Vinayagam, R.; Varadavenkatesan, T.; Selvaraj, R. Tetracycline Adsorption Research (2015–2025): A Bibliometric Analysis of Trends, Challenges, and Future Directions. *Results Eng.* **2025**, *27*, No. 106383.

(20) Yan, L.; Song, X.; Miao, J.; Ma, Y.; Zhao, T.; Yin, M. Removal of tetracycline from water by adsorption with biochar: A review. *J. Water Process Eng.* **2024**, *60* , No. 105215.

(21) Berradi, A.; Aziz, F.; Achaby, M. E.; Ouazzani, N.; Mandi, L. A comprehensive review of polysaccharide-based hydrogels as promising biomaterials. *Polymers* **2023**, *15* (13), No. 2908.

(22) Zhou, Q.; Kang, H.; Bielec, M.; Wu, X.; Cheng, Q.; Wei, W.; Dai, H. J. Influence of different divalent ions cross-linking sodium alginate-polyacrylamide hydrogels on antibacterial properties and wound healing. *Carbohydr. Polym.* **2018**, *197*, 292–304.

(23) Wang, H.; Huang, M.; Li, L.; Wang, B.; Jiang, C.; Hu, X.; Xie, Y.; Chen, R.; Guo, W.; Xiao, H.;et al. Air Highly efficient copper ions removal by sodium alginate/sodium humate@ Polyacrylamide: adsorption behavior and removal mechanism. *Water, Air, Soil Pollut.* **2024**, *235* (4), No. 250.

(24) Nazari, M. T.; Schnorr, C.; Rigueto, C. V.; Alessandretti, I.; Melara, F.; da Silva, N. F.; Crestani, L.; Ferrari, V.; Vieillard, J.; Dotto, G. L.; et al. A review of the main methods for composite adsorbents characterization. *Environ. Sci. Pollut. Res. Int.* **2022**, *29* (59), 88488–88506.

(25) Qin, Z.; Yang, Q.-L.; Cheng, X.-C.; Liu, H.-M.; Wang, X.-D. Structural features, chemical composition, antioxidant activities of organosolv lignins extracted from black and white sesame capsules and stalks. *Ind. Crops Prod.* **2021** *169*, No. 113677.

(26) Horseman, T.; Tajvidi, M.; Diop, C. I.; Gardner, D. J. Preparation and property assessment of neat lignocellulose nanofibrils (LCNF) and their composite films. *Cellulose* **2017**, *24*, 2455–2468.

(27) Bian, H.; Wei, L.; Lin, C.; Ma, Q.; Dai, H.; Zhu, J. Y.; Lignin-containing cellulose nanofibril-reinforced polyvinyl alcohol hydrogels. *ACS Sustainable Chem. Eng.* **2018**, *6* (4), 4821–4828.

(28) Xiao, T.; Hou, M.; Guo, X.; Cao, X.; Li, C.; Zhang, Q.; Jia, W.; Sun, Y.; Guo, Y.; Shi, H.; et al. Recent progress in deep eutectic solvent (DES) fractionation of lignocellulosic components: A review. *Renewable Sustainable Energy Rev.* **2024**, *192*, No. 114243.

(29) Tan, Y. T.; Chua, A. S. M.; Ngoh, G. C. Deep eutectic solvent for lignocellulosic biomass fractionation and the subsequent conversion to bio-based products–A review. *Bioresour. Technol.* **2020**, *297*, No. 122522.

(30) Li, P.; Yang, C.; Jiang, Z.; Jin, Y.; Wu, W. Bioproducts Lignocellulose pretreatment by deep eutectic solvents and related technologies: a review. *J. Bioresour. Bioprod.* **2023**, *8* (1): 33–44.

(31) Basak, B.; Patil, S.; Kumar, R.; Ha, G.-S.; Park, Y.-K.; Khan, M. A.; Yadav, K. K.; Fallatah, A. M.; Jeon, B.-H. Integrated hydrothermal and deep eutectic solvent-mediated fractionation of lignocellulosic biocomponents for enhanced accessibility and efficient conversion in anaerobic digestion. *Bioresour. Technol.* **2022**, *351* (351), No. 127034.

(32) Li, X.; Ning, C.; Li, L.; Liu, W.; Ren, Q.; Hou, Q. Fabricating lignin-containing cellulose nanofibrils with unique properties from agricultural residues with assistance of deep eutectic solvents. *Carbohydr. Polym.* **2021**, *274*, 118650.

(33) Liu, W.; Jiang, C.; Li, X.; Li, H.; Zhang, Y.; Huang, Y.; Chen, S.; Hou, Q. Microwave-assisted DES fabrication of lignin-containing cellulose nanofibrils and its derived composite conductive hydrogel. *Carbohydr. Polym.* **2024**, *328*, No. 121741.

(34) Suopajärvi, T.; Sirviö, J. A.; Liimatainen, H. Nanofibrillation of deep eutectic solvent-treated paper and board cellulose pulps. *Carbohydr. Polym.* **2017**, *169*, 167–175.

https://doi.org/10.1021/acssusresmgt.6c00244
ACS Sustainable Resour. Manage. XXXX, XXX, XXX–XXX

(35) Zhang, Z.; Lv, P.; Ji, H.; Ji, X.; Tian, Z.; Chen, J. Functional deep eutectic solvent for lignocellulose valorization via lignin stabilization and cellulose functionalization. *Green Chem.* **2024**, *26* (6), 3453–3465.
(36) Jeon, Y.; Lee, K.; Seo, Y.; Jung, J.; Lee, S.; Park, S.; Rim, H.; Kim, D.; Lee, J. T.; You, J. Lignin-tailored lignocellulose nanofiber films for light management using a deep eutectic solvent. *Chem. Eng. J.* **2025**, *520*, No. 165989.
(37) Kwon, G.-J.; Cho, S.-W.; Bandi, R.; Yang, B.-S.; Dadigala, R.; Han, S.-Y.; Ma, S.-Y.; Kim, J.-K.; Kim, N.-H.; Lee, S.-H. Production of lignocellulose nanofibrils by conventional and microwave-assisted deep-eutectic-solvent pretreatments: mechanical, antioxidant, and UV-blocking properties. *Cellulose* **2023**, *30* (7), 4277–4292.
(38) Li, H.; Liang, J.; Kong, F.; Ren, M.; Mohammed, A. E. A. Y.; Zhou, C. Preparation of lignin-containing cellulose nanofibers from walnut shell using deep eutectic solvent for nanotube conductive film. *Ind. Crops Prod.* **2024**, *207*, No. 117737.
(39) Li, C.; Zhou, M.; Liu, X.; Jiao, Y.; Chen, Y.; Jiao, G.; Sun, Q.; Zhang, F.; Sun, D. Tailored fractionation of lignin with low condensed structure and high yield using acidic ternary deep eutectic solvents based on a diol protection strategy. *Ind. Crops Prod.* **2025**, *230*, No. 121062.
(40) Zhao, X.; Lyu, G.; Meng, X.; Liu, Y.; Wang, Z.; Yoo, C. G. Novel ternary deep eutectic solvent fractionation for effective utilization of willow. *Bioresour. Technol.* **2024**, *407*, No. 131148.
(41) Narayanan, K.; Venkatachalam, P.; Panakkal, E. J.; Tantayotai, P.; Tandhanskul, A.; Selvasembian, R.; Chuetor, S.; Sriariyanun, M. Exploring Ternary Deep Eutectic Solvent Pretreatment in a One-Pot Process with Napier Grass for Bioethanol Production. *BioEnergy Res.* **2024**, *17*, 1–13.
(42) Haykir, N. I.; Viell, J.; Challenges and Opportunities for Gamma-Valerolactone in Biomass Pretreatment.*Ind. Eng. Chem. Res.* **2024**, *63* (28), 12251–12264.
(43) Valentini, F.; Brufani, G.; Di Erasmo, B.; Vaccaro, L. γ-Valerolactone (GVL) as a green and efficient dipolar aprotic reaction medium. *Curr. Opin. Green Sustainable Chem.* **2022** *36*, No. 100634.
(44) Morais, E. S.; Freire, M. G.; Freire, C. S.; Coutinho, J. A.; Silvestre, A. J. D. Enhanced conversion of xylan into furfural using acidic deep eutectic solvents with dual solvent and catalyst behavior. *ChemSusChem* **2020**, *13* (4), 784–790.
(45) Cheng, J.; Liu, X.; Huang, C.; Zhan, Y.; Huang, C.; Chen, T.; Meng, X.; Yoo, C. G.; Fang, G.; Ragauskas, A. J. Novel biphasic DES/GVL solvent for effective biomass fractionation and valorization. *Green Chem.* **2023**, *25* (16), 6270–6281.
(46) Yao, M.; Liu, B.; Qin, L.; Du, Z.; Wang, Z.; Qin, C.; Liang, C.; Huang, C.; Yao, S. Preparation of homogeneous lignin nanoparticles by efficient extraction of lignin and modification of its molecular structure using a functional deep eutectic solvent containing γ-valerolactone. *Green Chem.* **2024**, *26* (8), 4528–4543.
(47) Yu, S.; Qiu, B.; Jin, Y.; Zhao, Y.; Luo, W.; Qi, X. Efficient removal of lignin in tobacco stems with choline chloride-based deep eutectic solvents. *Ind. Crops Prod.* **2025**, *226*, No. 120634.
(48) Yan, B.; Fu, Y.; Ding, W.; Shi, G.; Wang, Z.; Zhang, S. Integrated dilute acid-ternary deep eutectic solvents treatment for efficient component separation and sugar platform from lignocellulose. *Ind. Crops Prod.* **2024**, *222*, No. 119808.
(49) Bessa, W.; Trache, D.; Tarchoun, A. F.; Abdelaziz, A.; Hussin, M. H.; Brosse, N. J. S. Unraveling the Effect of kraft and organosolv processes on the physicochemical properties and thermal stability of cellulose and its microcrystals produced from Eucalyptus globulus. *Sustainability* **2023**, *15* (4), No. 3384.
(50) Brazil, O. A. V.; Vilanova-Neta, J. L.; Silva, N. O.; Vieira, I. M. M.; Lima, Á. S.; Ruzene, D. S.; Silva, D. P.; Figueiredo, R. T. Integral use of lignocellulosic residues from different sunflower accessions: Analysis of the production potential for biofuels. *J. Cleaner Prod.* **2019**, *221*, 430–438.
(51) Gao, Y.; Ji, R.; Ren, Z.; Jiang, Z.; Xu, S.; Matharu, A. S. Insights into the Synergistic Mechanism of a Polyol-Assisted Ternary Deep Eutectic Solvent for the Production of Lignocellulosic Nanofibers and Lignin Nanoparticles from Sunflower Stalks. *ACS Sustainable Chem. Eng.* **2025**, *13*, 19586–19598.
(52) Han, S.; Wang, R.; Wang, K.; Jiang, J.; Xu, J. Low-condensed lignin and high-purity cellulose production from poplar by synergistic deep eutectic solvent-hydrogenolysis pretreatment. *Bioresour. Technol.* **2022**, *363*, No. 127905.
(53) Haykiri-Acma, H.; Yaman, S. Treating lignocellulosic biomass with dilute solutions at ambient temperature: Effects on cellulose crystallinity. *Biomass Convers. Biorefin.* **2022**, *14*, 9967–9981.
(54) Liao, J. J.; Abd Latif, N. H.; Trache, D.; Brosse, N.; Hussin, M. H. Current advancement on the isolation, characterization and application of lignin. *Int. J. Biol. Macromol.* **2020**, *162*, 985–1024.
(55) Değermenci, G. D.; Değermenci, N.; Ayvaoğlu, V.; Durmaz, E.; Çakır, D.; Akan, E. Adsorption of reactive dyes on lignocellulosic waste; characterization, equilibrium, kinetic and thermodynamic studies. *J. Cleaner Prod.* **2019**, *225*, 1220–1229.
(56) Bortoluz, J.; Cemin, A.; Bonetto, L. R.; Ferrarini, F.; Esteves, V. I.; Giovanela, M. J. C. Isolation, characterization and valorization of lignin from Pinus elliottii sawdust as a low-cost biosorbent for zinc removal. *Cellulose* **2019**, *26*: 4895–4908.
(57) Yu, Y.; Cheng, W.; Li, Y.; Wang, T.; Xia, Q.; Liu, Y.; Yu, H. Tailored one-pot lignocellulose fractionation to maximize biorefinery toward versatile xylochemicals and nanomaterials. *Green Chem.* **2022**, *24* (8), 3257–3268.
(58) Gao, Y.; Ozel, M. Z.; Dugmore, T.; Sulaeman, A.; Matharu, A. S. A biorefinery strategy for spent industrial ginger waste. *J. Hazard. Mater.* **2021**, *401*, No. 123400.
(59) Lu, H.; Zhang, L.; Yan, M.; Wang, K.; Jiang, J. Screw extrusion pretreatment for high-yield lignocellulose nanofibrils (LCNF) production from wood biomass and non-wood biomass. *Carbohydr. Polym.* **2022**, *277*, No. 118897.
(60) Kuznetsov, B.; Sudakova, I.; Garyntseva, N.; Skripnikov, A.; Pestunov, A.; Gnidan, E. J.; Birch wood biorefinery into microcrystalline, microfibrillated, and nanocrystalline celluloses, xylose, and adsorbents. *Wood Sci. Technol.* **2023**, *57* (1), 173–196.
(61) Chen, Y.; Fan, D.; Han, Y.; Lyu, S.; Lu, Y.; Li, G.; Jiang, F.; Wang, S. Effect of high residual lignin on the properties of cellulose nanofibrils/films. *Cellulose* **2018**, *25*, 6421–6431.
(62) Gao, Y.; Xia, H.; Sulaeman, A. P.; de Melo, E. M.; Dugmore, T. I.; Matharu, A. S. Engineering Defibrillated celluloses via dual twin-screw extrusion and microwave hydrothermal treatment of spent pea biomass. *ACS Sustainable Chem. Eng.* **2019**, *7* (13), 11861–11871.
(63) Yuan, T.; Zeng, J.; Wang, B.; Cheng, Z.; Chen, K. Lignin containing cellulose nanofibers (LCNFs): Lignin content-morphology-rheology relationships. *Carbohydr. Polym.* **2021**, *254*, No. 117441.
(64) Shapiro, A. J.; O'Dea, R. M.; Epps, T. H., III. Thermogravimetric analysis as a high-throughput lignocellulosic biomass characterization method. *ACS Sustainable Chem. Eng.* **2023**, *11* (49), 17216–17223.
(65) Zhao, D.; Feng, M.; Zhang, L.; He, B.; Chen, X.; Sun, J. Facile synthesis of self-healing and layered sodium alginate/polyacrylamide hydrogel promoted by dynamic hydrogen bond. *Carbohydr. Polym.* **2021** *256*, No. 117580.
(66) Yue, Y.; Wang, X.; Han, J.; Yu, L.; Chen, J.; Wu, Q.; Jiang, J. Effects of nanocellulose on sodium alginate/polyacrylamide hydrogel: Mechanical properties and adsorption-desorption capacities. *Carbohydr. Polym.* **2019**, *206*, 289–301.
(67) Huang, X.; Lee, C.-S.; Zhang, K.; Alhamzani, A. G.; Hsiao, B. S. Sodium alginate–aldehyde cellulose nanocrystal composite hydrogel for doxycycline and other tetracycline removal. *Nanomaterials* **2023**, *13* (7), No. 1161.
(68) Hu, X.-S.; Liang, R.; Sun, G. Super-adsorbent hydrogel for removal of methylene blue dye from aqueous solution. *J. Mater. Chem. A* **2018**, *6* (36), 17612–17624.
(69) Chen, X.; Liu, X.; Zhu, L.; Tao, X.; Wang, X. One-step fabrication of novel MIL-53 (Fe, Al) for synergistic adsorption-photocatalytic degradation of tetracycline. *Chemosphere* **2022**, *291*, No. 133032.
(70) Bi, J.; Zhang, Z.; Tian, J.; Huang, G. Interface engineering in a nitrogen-rich COF/BiOBr S-scheme heterojunction triggering efficient

https://doi.org/10.1021/acssusresmgt.6c00244
ACS Sustainable Resour. Manage. XXXX, XXX, XXX–XXX

photocatalytic degradation of tetracycline antibiotics. *J. Colloid Interface Sci.* **2024**, *661*, 761–771.
(71) Cheng, D.; Ngo, H. H.; Guo, W.; Chang, S. W.; Nguyen, D. D.; Zhang, X.; Varjani, S.; Liu, Y. Feasibility study on a new pomelo peel derived biochar for tetracycline antibiotics removal in swine wastewater. *Sci. Total Environ.* **2020**, *720*, No. 137662.
(72) Kasbaji, M.; Mennani, M.; Grimi, N.; Oubenali, M.; Mbarki, M.; Zakhem, H. E.; Moubarik, A. Adsorption of cationic and anionic dyes onto coffee grounds cellulose/sodium alginate double-network hydrogel beads: Isotherm analysis and recyclability performance. *Int. J. Biol. Macromol.* **2023** *239*, No. 124288.
(73) Tien, N. M.; Minh, D. T. C.; Nhung, T. N. C.; Khoa, T. D.; Hieu, N. H. Synthesis of biomass-derived cellulose carbon aerogel for tetracycline degradation via persulfate activation and energy storage. *Colloids Surf., A* **2025**, *727 part 1*, No. 138106.
(74) Zhang, X.; Lin, X.; He, Y.; Chen, Y.; Luo, X.; Shang, R. Study on adsorption of tetracycline by Cu-immobilized alginate adsorbent from water environment. *Int. J. Biol. Macromol.* **2019** *124*, 418–428.
(75) Luo, H.; Liu, Y.; Lu, H.; Fang, Q.; Rong, H. Efficient adsorption of tetracycline from aqueous solutions by modified alginate beads after the removal of Cu (II) ions. *ACS Omega* **2021** *6* (9): 6240–6251.
(76) Li, K.; Chen, M.; Chen, L.; Zhao, S.; Pan, W.; Li, P.; Han, Y. Adsorption of tetracycline from aqueous solution by ZIF-8: Isotherms, kinetics and thermodynamics. *Environ. Res.* **2024**, *241*, No. 117588.
(77) Ngoc, D. M.; Hieu, N. C.; Trung, N. H.; Chien, H. H.; Thi, N. Q.; Hai, N. D.; Chao, H.-P. Tetracycline removal from water by adsorption on hydrochar and hydrochar-derived activated carbon: performance, mechanism, and cost calculation. *Sustainability* **2023**, *15* (5), No. 4412.
(78) Tang, X.; Huang, Y.; He, Q.; Wang, Y.; Zheng, H.; Hu, Y. Adsorption of tetracycline antibiotics by nitrilotriacetic acid modified magnetic chitosan-based microspheres from aqueous solutions. *Environ. Technol. Innovation* **2021**, *24*, No. 101895.
(79) Liao, Q.; Rong, H.; Zhao, M.; Luo, H.; Chu, Z.; Wang, R. Strong adsorption properties and mechanism of action with regard to tetracycline adsorption of double-network polyvinyl alcohol-copper alginate gel beads. *J. Hazard. Mater.* **2022**, *422*, No. 126863.

https://doi.org/10.1021/acssusresmgt.6c00244
ACS Sustainable Resour. Manage. XXXX, XXX, XXX–XXX